



LAWRENCE
LIVERMORE
NATIONAL
LABORATORY

Silicide Characterization at Alumina-Niobium Interfaces

J. T. McKeown, V. R. Radmilovic, R. Gronsky, A.
M. Glaeser

September 17, 2010

Journal of Materials Science

Disclaimer

This document was prepared as an account of work sponsored by an agency of the United States government. Neither the United States government nor Lawrence Livermore National Security, LLC, nor any of their employees makes any warranty, expressed or implied, or assumes any legal liability or responsibility for the accuracy, completeness, or usefulness of any information, apparatus, product, or process disclosed, or represents that its use would not infringe privately owned rights. Reference herein to any specific commercial product, process, or service by trade name, trademark, manufacturer, or otherwise does not necessarily constitute or imply its endorsement, recommendation, or favoring by the United States government or Lawrence Livermore National Security, LLC. The views and opinions of authors expressed herein do not necessarily state or reflect those of the United States government or Lawrence Livermore National Security, LLC, and shall not be used for advertising or product endorsement purposes.

SILICIDE CHARACTERIZATION AT ALUMINA-NIOBIUM INTERFACES

J.T. MCKEOWN^{A,C,*}, V.R. RADMILOVIC^B, R. GRONSKY^C, AND A.M. GLAESER^C

^A *Condensed Matter and Materials Division, Lawrence Livermore National Laboratory, Livermore, CA 94550, USA*

^B *National Center for Electron Microscopy, Lawrence Berkeley National Laboratory, Berkeley, CA 94720, USA*

^C *Department of Materials Science & Engineering, University of California, Berkeley, CA 94720, USA*

KEYWORDS: Joining, ceramics, metals, interfaces, silicides, TEM

ABSTRACT

Alumina-niobium interfaces formed by liquid-film-assisted joining with copper/niobium/copper interlayers exhibited microstructures that depend on the nature of the alumina components. Characterization of these interfaces in the transmission electron microscope provided insight on the relationship between interfacial microstructure and fracture performance. Interfaces between sapphire and niobium and those between high-purity (99.9%) polycrystalline alumina and niobium were free of secondary phases. However, niobium silicides were found at interfaces between lower-purity (99.5%) alumina and niobium, identified by electron diffraction analysis as the body-centered tetragonal α -Nb₅Si₃ phase. Spatially resolved compositional analysis was conducted on silicide particles at and away from the interface.

* Corresponding author. Email: mckeown3@llnl.gov

1. INTRODUCTION

The formation of secondary phases plays an important role in both the processing and properties of fabricated ceramic-metal interfaces. Alumina (Al_2O_3)-niobium (Nb) interfaces represent a model ceramic-metal system, where the effects of interface chemistry have been studied [1-7] and interfacial Nb silicides have been previously observed [3, 6, 7] as a result of the flow of a glassy silicate phase along grain boundaries in Al_2O_3 to the interface during bonding. The combination of polycrystalline Al_2O_3 and polycrystalline Nb, and their contact along an interface, results in a wide range of potential nucleation sites for silicide formation. These include Nb-Nb, Al_2O_3 - Al_2O_3 , and Al_2O_3 -Nb grain boundaries, triple junctions involving either two Al_2O_3 or two Nb grains, and four-grain corners involving Al_2O_3 triple lines or Nb triple lines. Each type of site has a distinct spatial density and a distinct nucleation barrier that will combine to define a spectrum of nucleation frequencies. The site providing the optimum combination of energetics and spatial density will have the highest overall nucleation rate [8]. Growth rates will be influenced by the site-specific diffusion paths and Si availability, and in conjunction with nucleation rates, will determine the nature of the site or sites that dominates the overall distribution of reaction products. The properties and microstructure of such reaction products, Nb silicides in the case of interest here, can, in turn, influence the fracture path and fracture energy.

Silicide Formation

Studies of Nb silicide nucleation generally involve planar “bulk” reaction couples or planar “thin-film” couples produced by depositing thin Nb films onto single-crystal Si substrates, which are subsequently annealed at various temperatures. Rules have been formulated to predict first-phase nucleation and the subsequent sequence of phase formation in binary metal-Si thin-film systems [9-11]. Based on the equilibrium phase

diagram and consideration of the interfacial energies that appear in the nucleation barrier to silicide formation [9, 11] it has been predicted that the first crystalline silicide phase to form in the Nb-Si system will be NbSi₂ (Figure 1 gives the Nb-Si binary equilibrium phase diagram [12]). An effective heat of formation concept [13-16] making direct use of thermodynamic data has been successful in predicting silicide phase-formation sequences in multiple metal-Si systems, as well as explaining how the presence of impurities can alter this sequence.

Experimentally, the nature of the phase(s) formed even in the Nb-Si binary system depend upon the nature of the experiment performed, *e.g.*, a thin film versus bulk reaction couple, the specific anneal time and temperature. In thin-film studies, Nb₃Si was the first phase to nucleate during deposition of Nb-Si multilayers onto single-crystal Si substrates prepared by ion-beam sputtering between 180C and 500°C [17, 18]. In contrast, amorphous Nb silicides of varying composition were formed during depositions at room temperature and 560°C. Anneals at 550°C produced Nb₅Si₃ and NbSi₂ with amorphous silicide, while anneals at 700°C produced only NbSi₂. This phase-formation sequence was attributed to the mobility of Si, and the phase sequence agreed with that predicted by calculated effective heats of formation [16]. When alternating layers of Nb and an amorphous Nb silicide were sputter-deposited at room temperature and subsequently annealed at elevated temperatures [19], the first silicide phase to form between 740°C and 800°C was Nb₅Si₃. Upon heating to 1000°C metastable Nb₃Si was formed with Nb₅Si₃. The metastable phase was eliminated by continued annealing at 1200°C. In bulk materials with quasiperiodic two-phase structures such as those that develop locally in dendritic structures, metastable phases can also be found. Metastable orthorhombic Nb₃Si precipitates have been reported within the Nb-rich phase in a Nb-14 at.% hypoeutectoid alloy [20]; a reduced nucleation barrier due to a low interfacial energy orientation relationship between the metastable Nb₃Si and the bcc Nb-rich matrix was suggested as the basis for forming the metastable phase. More recently, a body-

centered orthorhombic phase, thought to be metastable, was found as a precipitate in Nb-Si solid solution containing from 16–25 at.% Si [21]. The crystal structure was determined using crystallographic analysis of data obtained in the transmission electron microscope (TEM) combined with first-principles calculations.

In thin-film (and other periodic) systems, interpretation can be difficult due to limited amounts of one or more components, phases forming sequentially rather than simultaneously, and the effects of interfaces on growth and diffusion [22]. To avoid these complications, *bulk* diffusion couples of Nb-Si and Nb-NbSi₂ were used to study diffusion-controlled reactive growth of NbSi₂ and Nb₅Si₃ in the temperature range 1200–1350°C [22]. Anneal times ranged from 2–24 h. In Nb-Si couples, NbSi₂ nucleated first and grew much faster than the Nb₅Si₃ layer that developed (the NbSi₂ layer was ≈1 order of magnitude thicker than the Nb₅Si₃ layer). In both diffusion couples, an Nb₅Si₃ layer developed between the Nb and NbSi₂. Preliminary experiments showed that the growth rate of Nb₅Si₃ was very low at temperatures below 1200°C and obtaining a layer a few microns in thickness required very long anneal times.

It is to be expected that as systems under consideration become more chemically complex, further complexities can arise in the phase-formation preferences and sequences. In the interlayer used for joining, Cu is a minor constituent concentrated near the interface between the Nb-rich interlayer and a potentially silicate-containing Al₂O₃. This renders the Nb-Si-Cu system of interest.

The ternary Nb-Si-Cu system has been investigated in both thin-film reaction couples [23] and “bulk” phase-equilibria studies [24, 25]. In the thin-film study, bilayers of Nb-Cu or Cu-Nb were deposited on Si(100) using electron-beam evaporation and annealed for 30 min at temperatures between 200°C and 800°C [23]. In the Nb/Cu/Si(100) system, the Cu deposited epitaxially on the Si substrate, while the Nb was polycrystalline. A layered growth process was observed, resulting in a (NbSi₂+Nb₅Si₃)/Cu₃Si/Si structure after anneals at 700°C. Annealing at higher

temperatures led to intermixing of the silicides and the formation of $\text{Nb}_5\text{Cu}_4\text{Si}_4$. For the Cu/Nb/Si(100) system, both the Nb and Cu layers were polycrystalline. Interdiffusion at both the Cu-Nb and Nb-Si interfaces began at 400°C and the ternary $\text{Nb}_5\text{Cu}_4\text{Si}_4$ phase formed at 700°C . At 800°C the ternary phase was found along with NbSi_2 , Nb_5Si_3 , and a small amount of Cu_4Si . The presence of Cu at the Nb-Si interface was found to affect the onset temperature for Nb_3Si and Nb_5Si_3 formation.

Isothermal sections of the ternary Nb-Si-Cu phase diagram are available at 1500°C , 875°C , and 800°C . Figure 2 shows the 1500°C isothermal section. It should be noted that, according to the Nb-Cu binary phase diagram [12], there is very low solubility of Cu in Nb and Nb in Cu. Alloys investigated using microprobe analysis exhibited no measurable amounts of Nb in the Cu-rich Cu_3Si phase [25]. The Nb_5Si_3 and NbSi_2 phases dissolved ≈ 4 at.% Cu in the temperature range 800 – 875°C . The ternary $\text{Nb}_5\text{Cu}_4\text{Si}_4$ was only formed upon rapid cooling from the melt or by solid-state diffusion (as occurred in the thin-film diffusion couples). The tetragonal $\text{Nb}_5\text{Cu}_4\text{Si}_4$ had previously been observed at 800°C [26] and confirmed in a later study [24]. A tetragonal Nb_4CuSi has been observed at 1500°C , in equilibrium with pure Nb and Nb_5Si_3 [24].

In the system used in this study, some dissolution of Al_2O_3 can occur in the presence of Nb at elevated temperatures, and as a result, there is interest in potential effects of Al as an impurity on phase-formation preferences and sequences. Phase-equilibria studies of the ternary Nb-Si-Al system [27-31] indicated the formation of the ternary compounds $\text{Nb}_3\text{Si}_5\text{Al}_2$ and $\text{Nb}_{10}\text{Si}_3\text{Al}_3$. It was determined [31] that the “ternary” $\text{Nb}_{10}\text{Si}_3\text{Al}_3$ phase was actually the binary $\beta\text{-Nb}_5\text{Si}_3$ phase stabilized to lower temperatures by the addition of Al, making this phase $\beta\text{-Nb}_5(\text{Si},\text{Al})_3$. The solubility of Al in $\alpha\text{-Nb}_5\text{Si}_3$ was found to be ≈ 3 at.% at 1400°C [27], while at 1500°C it was suggested to be ≈ 12 at.% [30] and at 1000°C it was shown to be ≈ 8 at.% [31]. Although the solubility of Al in $\alpha\text{-Nb}_5\text{Si}_3$ varies with temperature, it is only ≈ 3 – 5 at.% when the silicide is in equilibrium

with the pure Nb phase, leading to the formation of the Nb₃Al phase in the ternary system when the Al solubility is above ≈ 3 at.% [31].

Mechanical Properties

In idealized systems in which two phases are in contact and form bimaterial interfaces, thermal-expansion mismatches can establish residual stresses that alone or in combination with applied stresses cause failure at or near the interface (see, *e.g.*, [32]). Even when the coefficients of thermal expansions (CTEs) are closely matched, as is the case for the combination of Al₂O₃ and Nb, differences in other physical properties will affect the fracture path and resulting fracture energy.

Fracture at a bimaterial interface is generally described by the complex stress-intensity factor [33-35], K , in which the elastic mismatch across the interface is expressed using the nondimensional Dundurs parameters [36], α and β . The Dundurs parameters are functions of the elastic moduli, Poisson's ratios, and shear moduli of the two materials. It was noted by Kruzic *et al.* [6] that in sandwich-type specimens, for which complex stress-intensity solutions exist [37], analysis is complicated by deviations of cracks from the interface [38] and the validity of these solutions breaks down at distances ahead of the crack tip [39]. Using the strain energy release rate, G , in mode I loading to evaluate crack driving forces [6] avoids these complications. In addition, G is easy to compute, invariant with respect to crack position, and unaffected by the presence of the interlayer in sandwich specimens when the interlayer thickness is small compared with other relevant specimen dimensions [37].

Cannon *et al.* [40, 41] found that while linear-elastic calculations predict crack propagation along a path with maximum G and to be dependent on the Dundurs parameters (modulus mismatch), this analysis was limited in bimaterial systems. Engineering interfaces with enhanced toughness involves generating plasticity in the metal interlayer, the competition between microstructurally weak crack paths and paths

of maximum driving force, and encouraging crack jumping across the metal interlayer and crack meandering. At Al_2O_3 -Nb interfaces, it is expected that cracks that initiate close to the interface will be drawn to the Nb interlayer. The detailed crack path and fracture energy will depend on interlayer thickness and yield strength, as well as microstructural and chemical characteristics of the interface.

In the samples employed in the current study, Nb silicides along the ceramic-interlayer interface have the potential to provide microstructural weak links and can generate localized residual stresses that interact with an advancing crack. Nb silicides are brittle at room temperature. Vickers hardness values of 5.6–9.5 GPa [42] and K_{IC} values of 2.3–5.5 $\text{MPa}\sqrt{\text{m}}$ [42, 43] were measured for pure Nb_5Si_3 samples. If one assumes an elastic modulus of 188 GPa for Nb_5Si_3 [44], the K_{IC} values would imply mode I fracture energies, G_{IC} , of 28–161 J/m^2 . Investigations of the fracture energy of heterophase interfaces involving Nb silicide [45] found the interfacial fracture energy of Al_2O_3 with Nb_5Si_3 to be $\approx 16 \text{ J}/\text{m}^2$, while the interfacial fracture energy between Nb and Nb_5Si_3 was found to exceed 34 J/m^2 .

Effects of Silicides at Processed Interfaces

Even in a “simple” system such as Nb-Si, a range of phases and phase distributions develop in multilayer systems. The associated microstructural differences have the potential to induce differences in the response to loading, specifically, the fracture path and fracture energy.

In the Al_2O_3 -Nb system, the potential Si source is an intergranular glassy phase in the Al_2O_3 . In fracture studies of Al_2O_3 -Nb interfaces in which the Al_2O_3 was heavily contaminated with silicate (97%-pure Al_2O_3) [3], Nb embrittlement due to oxygen uptake was augmented relative to assemblies using higher-purity Al_2O_3 by flow of Si/silicate to the Al_2O_3 -Nb interface. Patches of Nb silicide (Nb_4Si) were identified on fracture

surfaces of specimens that failed within the Nb. These silicide patches extended into the Nb in the vicinity of the Al₂O₃-Nb interface.

In studies of Al₂O₃-Nb interfaces fabricated with Cu/Nb/Cu interlayers, the processing conditions and Al₂O₃ purity influence the interfacial microstructure and failure behavior. For 99.5% Al₂O₃ bonded at 1150°C, beams failed almost exclusively along the Al₂O₃-interlayer interface [46]. The fracture path included excursions into the Al₂O₃, causing localized pullout of Al₂O₃ grains, but the pullouts appeared to be linked to the locations of interfacial Cu particles rather than silicides. The results suggest that if an interfacial silicide phase formed during bonding at 1150°C, it was a more minor factor in the failure. An additional 10-h post-bonding anneal at 1000°C of already sectioned beams in high-purity Ar oxygen-gettered with a mixture of Ti and Zr chips increased the amount of Al₂O₃ pullout and significantly increased Si levels were reported around the perimeter of the pullout zones [46]. This may reflect changes in the extent of reaction, possibly assisted by the reduced ambient O₂ pressure and reduced diffusion distance relative to the full block dimension.

An increase in the processing temperature from 1150°C to 1400°C [47] increased the average fracture strength of bonded assemblies from 180 MPa to 240 MPa, and shifted the fracture path from 100% interfacial failures to 75% ceramic failures. It is tempting to attribute this shift to a change in interfacial microstructure. The increase in bonding temperature is expected to accelerate Al₂O₃-Nb interface formation, increase the degree of redistribution and breakup of the initially continuous Cu film, facilitate flow of silicate, and increase the extent of reaction between the Nb and silicate. Post-bonding anneals of beams at 1000°C in a gettered-Ar atmosphere for a period from 5–220 h revealed a decrease in fracture strength and a clear shift back to interfacial failures with increasing anneal time; comparable duration anneals in a vacuum environment resulted in no obvious strength degradation and no shift in the fracture path.

Further studies of 99.5% Al₂O₃ bonded at 1400°C with Cu/Nb/Cu interlayers [48] showed that varying the Cu film thickness affected the fracture path, with 0- μ m and 1.4- μ m Cu films yielding all interfacial failures with localized tearing of the interlayer in the finer-grain regions of the alumina, and 3- μ m-thick layers shifting the fracture path to the ceramic in 75% of the tests. A further increase of the Cu film thickness to 5.5 μ m [49] resulted in increased scatter and an increased fraction of interfacial failures relative to joints processed with a 3- μ m-thick Cu film.

An assessment of the fracture and fatigue behavior of bonded assemblies [6] approximated the system as a bimaterial system. In view of the relative amounts of Al₂O₃, Nb, and Cu, the mismatches in modulus and CTE between Al₂O₃ and Nb were thought to be the most relevant. Fracture toughness tests indicated precracks that were partially in the alumina were drawn to the Al₂O₃-interlayer interface, and under monotonic loading, fracture proceeded largely along the interface, with ductile tearing of bridging Cu particles. Adherent Nb₅Si₃ particles were observed on the Al₂O₃ side of the fracture surfaces, but accounted for a relatively small fraction of the fracture surface. In contrast, when fatigue tests were performed, excursions of the crack into the ceramic were much more prevalent, with between 50–100% of the interlayer side of the interface covered with adherent Al₂O₃ grains.

These collective observations indicate a substantial sensitivity of the fracture behavior to the processing temperature, bonding atmosphere, interlayer design, post-bonding heat treatments, and testing method even in situations where, from a macroscopic perspective, the system is approximated as an Al₂O₃-Nb bond (a bimaterial interface) and the *same* Al₂O₃ is used throughout. This suggests that the interfacial microstructure is sensitive to the details of the processing, and that changes in the processing parameters, broadly defined, influence the interplay between fracture paths of maximum driving force and those of microstructural weakness. Changes in the nature of the Al₂O₃ add further complexity. This work was undertaken in part to more fully

characterize the nature of the ceramic-metal interfaces generated, particularly the interface between an Al_2O_3 containing an intergranular glassy phase and a Nb-based interlayer, and relate the observed microstructures to the fracture characteristics of the interfaces.

2. EXPERIMENTAL PROCEDURES

The materials and experimental procedures used to produce samples for the characterization studies described herein are identical to those used in prior studies to produce joined samples with Cu/Nb/Cu interlayers. Three types of Al_2O_3 were used: an undoped, high-purity, single-crystal, (0001)-oriented sapphire ($\approx 99.996\%$ pure, Insaco Inc., Quakertown, PA, USA); a high-purity, high-strength, fine-grain-size polycrystalline Al_2O_3 ($\approx 99.9\%$ pure, SSA-99W, Nikkato Corp., Osaka, Japan); and a lower-purity, lower-strength, coarser-grain-size polycrystalline Al_2O_3 ($\approx 99.5\%$ pure, AD995, Coors Technical Ceramic Co., Oak Ridge, TN, USA). The 99.9% pure material had a uniform microstructure with an average (mean linear intercept) grain size of $\approx 1 \mu\text{m}$; the 99.5% pure Al_2O_3 exhibited a bimodal grain-size distribution, with the larger grains roughly $25 \mu\text{m}$ in size and the finer-grained regions typically consisting of grains $\approx 5 \mu\text{m}$ or less in size. The manufacturer polished the sapphire to an optical finish. Surface roughness measurements using contact profilometry yielded average R_a values of 0.0036, 0.0037, and $0.0108 \mu\text{m}$ for line scans of 50, 500, and $5000 \mu\text{m}$, respectively. The bonding surfaces of polycrystalline Al_2O_3 blocks were first ground flat with a 400-grit ($37\text{-}\mu\text{m}$) diamond wheel, then polished with successively finer-grit diamond (9-, 6-, 3-, $1\text{-}\mu\text{m}$) paste and finished with $0.02\text{-}\mu\text{m}$ colloidal silica suspension. For the polycrystalline samples, average R_a values for line scans of 50, 500, and $5000 \mu\text{m}$ were 0.0089, 0.0105, and $0.0784 \mu\text{m}$, respectively. The polished surfaces of the Al_2O_3 substrates were coated with $\approx 3.0\text{-}\mu\text{m}$ -thick Cu films. The coated Al_2O_3 substrates were joined using a $125\text{-}\mu\text{m}$ -

thick Nb foil ($\approx 99.99\%$ pure, Goodfellow Corp., Malvern, PA, USA) in a graphite-element hot press. A bonding pressure of ≈ 2 MPa was maintained for 6 h at 1400°C under a vacuum of $\approx 10^{-2}$ Pa (10^{-7} atm). In-depth processing details are available in previous publications [46-51].

Cross-sectional TEM specimens of the interfaces were prepared by conventional grinding, polishing, and dimpling techniques after the interface cross-sections were mounted in 3-mm-diameter Al_2O_3 -tube assemblies. The thin foils were perforated using a low-energy Ar^+ ion mill. Conventional TEM (imaging and diffraction analysis) was performed on a JEOL 200CX and a JEOL 2011 operating at 200 keV. Elemental analysis using energy-dispersive spectrometry (EDS) was performed on a Philips CM200 FEG (S)TEM operating at 200 keV with a probe size of 2 nm.

3. RESULTS AND DISCUSSION

The solubility-diffusivity product for Cu in Nb is sufficiently low at the bonding temperature (1400°C) that, for a bonding time of 6 h, discrete particles of residual Cu decorate the sapphire-Nb and Al_2O_3 -Nb interfaces. The morphology and projected (plan-view) area fraction of these ductile interfacial Cu particles influence the extent of toughening obtained through metal plasticity and particle tearing, and thereby affect the fracture strength of the joined assemblies [6, 7, 45, 48, 52]. The ultimate spatial distribution of Cu along the ceramic-interlayer interface will depend upon the bonding temperature, pressure, and time, the bonding-surface roughness, and the microstructure and chemistry of the bulk ceramic [7, 47-50, 53]. Well-polished samples with R_a much less than the Cu film thickness, fabricated using the same bonding conditions, were selected to isolate the effects of Al_2O_3 microstructure and purity.

Prior work has shown that in all three types of samples, the area fraction of residual Cu particles at the ceramic-interlayer interface is typically $\leq 5\%$ for the

processing conditions described. As a result, a plan view of the ceramic-interlayer interface is well suited to detecting and characterizing the Cu particle size and distribution. Comparisons of sapphire-interlayer interfaces and polycrystalline Al_2O_3 -interlayer interfaces reveal that the sizes and distributions of particles are affected by the ceramic microstructures. Specifically, the average size of Cu particles, and to a lesser degree the projected area fraction, decreases with the grain size. This, coupled with observations of the fracture-surface topography, suggests that grain-boundary grooving in both the metal foil [7, 50] and on the ceramic surface plays a role in defining the average size and spacing of the Cu particles. Decreasing the average Cu particle size will in turn increase the amount of Cu-interlayer contact area per unit area of interface, which may increase the total flux of Cu into the Nb core layer and contribute to decreasing area fractions of Cu with decreasing Al_2O_3 grain size.

As a result of the low area fraction of Cu particles, assumed to be ≤ 0.05 , the average nearest-neighbor particle separation distance is estimated to be of the order of $\geq 3-5 \times$ the average particle diameter ($\approx 10 \mu\text{m}$ in samples using sapphire substrates to $\leq 1 \mu\text{m}$ in samples using high-purity Al_2O_3 substrates). A *random* cut perpendicular to the plane of the interface, designed to allow a cross-sectional view, will generally intersect relatively few and widely separated particles. In an SEM, it is possible to view in cross-section an interface that is multiple millimeters in length, and those segments in which particles are intersected can be examined. In the TEM work described here, a typical length of ceramic-interlayer interface is in the range of 2–20 μm . It follows that the likelihood of a particle intersection is very low. This is consistent with our observations (or lack thereof). Moreover, due to the relatively higher milling rate of Cu, even when Cu particles are intersected, there is a high likelihood that preferential etching of a through-thickness particle will generate a particle-shaped perforation along the ceramic-interlayer interface. Isolated observations of such features have been made.

In view of the understandable absence of Cu particles, the primary differences in the interfacial microstructures and chemistries among the three types of samples fabricated reflect the effects of the Al_2O_3 microstructure on the interface “roughness” and of the Al_2O_3 chemistry on Al_2O_3 -interlayer compatibility and the potential for reaction-product formation along the interface. Figure 3 presents bright-field TEM images of the three types of fabricated interfaces for comparison of the microstructures.

Figure 3(a) shows a (0001) sapphire–Nb interface. The interface appears distinct and smooth with no reaction phases present [2, 50, 54, 55], as sapphire eliminates the possibility of a glassy phase flowing to and filling interfacial voids [50]. EDS confirmed that silicides and other secondary phases were not present at the sapphire-Nb interface.

Figure 3(b) shows a bright-field TEM image of a high-purity Al_2O_3 –Nb interface. Again, there was no evidence of silicide or other secondary-phase formation at the interface, as expected for a high-purity Al_2O_3 . EDS confirmed this. The interface appears “rough” relative to the sapphire-Nb interface due to grooving of the fine-grained Al_2O_3 during the bonding cycle, with the Nb conforming to the Al_2O_3 grain-boundary grooves. This roughness was even more evident in fracture surfaces when joined assemblies prepared from this Al_2O_3 failed along the ceramic-interlayer interface [50]. As observed in previous studies [56-58], preferential thinning of the interface occurs during TEM specimen preparation.

Figure 3(c) reveals the microstructure along a lower-purity Al_2O_3 –Nb interface. Again, the Nb has conformed to the Al_2O_3 grain-boundary grooves, and the interface appears “rough” relative to the single-crystal sapphire–Nb interface. Nb silicides are evident at and slightly away from the Al_2O_3 -Nb interface, consistent with previous studies [6, 7] in which Nb-silicide formation was observed in small-grained regions of the Al_2O_3 . This higher grain-boundary density in these regions leads to a higher flux and local concentration of Si per unit area of Al_2O_3 at the interface as the glassy silicate phase present at Al_2O_3 grain boundaries flows to the interface. Chemical analysis using EDS [6,

7] indicated a Nb:Si ratio of $\approx 4.5/3$ (≈ 1.5) and the silicide particles were determined to be the Nb_5Si_3 phase (see Figure 1). At these interfaces, nucleation likely occurred where Nb metal was in contact with Al_2O_3 grain boundaries, and thus silicate that flowed to the interface. Silicide formation requires a sufficiently low O_2 activity; the equilibrium O_2 partial pressure to form Nb_5Si_3 from a reaction between pure SiO_2 and Nb is of the order of 10^{-14} atm (10^{-9} Pa) at 1400°C . The O_2 partial pressure for Nb-NbO equilibrium at 1400°C is $\approx 6 \times 10^{-18}$ (6×10^{-13}) atm at 1400°C [59]. The Nb foil is thus expected to establish a low O_2 activity along the Al_2O_3 -Nb interface, which in turn promotes the reaction of an intergranular silicate with Nb to form a silicide in the near-interfacial region. Moreover, oxygen readily dissolves in and is a fast diffuser in Nb [60, 61]. The dissolution makes the reaction more favorable, and the rapid diffusion prevents a build-up of dissolved oxygen at the interface. The graphite-element environment coupled with a 10^{-7} atm (10^{-2} Pa) vacuum pressure during bonding is expected to establish a sufficiently low ambient O_2 pressure to allow oxygen removal from the foil edges. Under these conditions, the observed formation of interfacial silicides is expected.

The local microstructure seen in Figure 3(c) suggests that following nucleation the particles grew into the Al_2O_3 along grain boundaries, where the Si concentration will be higher as the reaction progresses. The silicide particles also grew laterally along the Al_2O_3 -Nb interface and slightly into the Nb. Lateral expansion of the silicide along the Al_2O_3 -Nb interface is likely due to enhanced diffusion of Si along the Al_2O_3 -silicide boundary or flanking Al_2O_3 -Nb boundary, as the rate of diffusion along this boundary can be expected to be much greater than diffusion of Si through the silicide lattice. Faceting at the interface between Nb and the Nb silicide was observed (see, for example, Figure 7(a)), which may limit the growth rate of the silicide into the Nb foil. Grain boundaries in the silicide particles suggest multiple nucleation sites along Al_2O_3 grain boundaries.

Chemical analysis was performed on silicide particles at and away from the Al_2O_3 -Nb interface using EDS in the TEM. Figure 4(a) shows EDS spectra obtained from

multiple regions of a silicide particle at the interface. The spectra show the presence of Nb, Si, and Cu, and no dissolved Al in the particle. When the spectra are normalized by their maximum Nb_L counts to reduce specimen-thickness effects, the normalized spectra overlap, indicating constant Nb:Si and Nb:Cu ratios in the silicide particle. Figure 4(b) presents an EDS line scan across the silicide particle. The dashed line in the figure indicates the position of the interface between the Nb metal and silicide particle. The interface does not appear distinct due to the combined effects of specimen thickness and tilting of the interface (the interface is not edge-on) relative to the incident electron beam. Minimizing these thickness effects was again achieved by normalizing the Cu and Si counts by the Nb counts at each position in the scan. The Nb:Si and Nb:Cu ratios appear constant across the silicide particle. The nominal composition of this particle was 54(± 2) at.% Nb, 40(± 2) at.% Si, and 6(± 5) at.% Cu, with a Nb:Si ratio of 1.35. The presence of dissolved Cu is a result of the cladding layers of the interlayer used to join the Al_2O_3 .

Small, isolated particles on Al_2O_3 grain boundaries away from the Al_2O_3 -Nb interface, believed to have formed during cooling from the processing temperature [7], were also analyzed. Figure 5 shows an EDS line scan across a particle that lies $\approx 1 \mu m$ from the Al_2O_3 -Nb interface, with the associated HAADF image. The EDS scan again reveals the presence of Nb, Si, and trace amounts of Cu. Figure 6 shows an EDS spectrum obtained from a particle ≈ 500 nm from the Al_2O_3 -interlayer interface. The nominal composition of the particle was 52(± 4) at.% Nb, 43(± 4) at.% Si, and 5(± 10) at.% Cu, giving a Nb:Si ratio of 1.21. The accuracy of compositions obtained from particles along Al_2O_3 grain boundaries are likely skewed by the Al_2O_3 that partially envelops the silicide particle, which produced Al and O signals, as seen in Figure 6, along with Nb, Si, and Cu. The uncertainty in the estimated Cu level is perhaps symptomatic of the difficulties. In view of this, the shift in the Nb:Si ratio to 1.21 relative to that of the silicides closer to the Al_2O_3 -interlayer interface (Nb:Si of 1.35) must be viewed with caution.

In order to accurately determine the specific Nb-silicide phase, crystallographic analysis was conducted using electron diffraction. Based on the Nb:Si ratios, which will be further discussed subsequently, attention turned to the Nb₅Si₃ phase. There are two stable allotropes of Nb₅Si₃, both with a body-centered tetragonal crystal structure (space group I4/mcm): α -Nb₅Si₃ is stable below 1940°C with lattice parameters $a=6.571$ Å and $c=11.889$ Å while β -Nb₅Si₃ is stable above 1650°C with lattice parameters $a=10.018$ Å and $c=5.072$ Å [12, 62, 63]. Metastable γ -Nb₅Si₃ is hexagonal (space group P6₃/mcm) with lattice parameters $a=7.536$ Å, $c=5.249$ Å, and $\gamma=120^\circ$ and has been found to be stabilized by interstitial impurities, particularly C [62, 63]. As a specific example of stabilization by interstitial impurities, the addition of Hf was found to stabilize γ -Nb₅Si₃ up to 1500°C [64]. At the processing temperature employed in this study, NbSi₂, with a hexagonal crystal structure (space group P6₂22) and lattice parameters $a=4.819$ Å, $c=6.592$ Å, and $\gamma=120^\circ$, is also stable [63]. In diffusion couples involving bulk Nb/Si and bulk Nb/NbSi₂ phases in the temperature range from 1200–1350°C, only NbSi₂ and Nb₅Si₃ formed [22]. Similarly, in samples prepared by field-activated pressure-assisted combustion synthesis of elemental Nb and Si powders at 1400°C, either Nb₅Si₃ or a combination of Nb₅Si₃ and NbSi₂ were formed [42]. We note that reports of multiple other phases exist in the literature, but the phases appear in samples processed either at higher or lower temperatures. Nb₃Si appears in the binary phase diagram between 1770°C and 1980°C, and both stable tetragonal primary Nb₃Si [20, 65] and finer metastable orthorhombic Nb₃Si particles [20] have been observed in solidified materials, but these materials were processed at higher temperatures than the joints produced for this study. A body-centered orthorhombic Nb₁₁Si₄ [21] phase has recently been reported to form as a precipitate in Nb-Si solid solutions. The tetragonal Nb₅Cu₄Si₄ phase has been reported in both phase-equilibria studies [24] and thin-film reaction couples [23] processed at temperatures lower than the bonding temperature used in the present work.

Additionally, tetragonal Nb₄CuSi [24] has been observed. Consequently, it was desirable to identify the crystallographic form(s) of the silicides in our material.

The silicide particle shown in Figure 4, from which EDS data was obtained, was chosen for crystallographic analysis. The lateral expansion of the silicide particle at the interface decreases the likelihood of surrounding Al₂O₃ or Nb either above or below the silicide through the thickness of the TEM foil. The bright-field image in Figure 7(a) shows the silicide particle, recorded in the [001] zone axis. There was no low-index plane-on-plane orientation relationship between this silicide and Nb pair, nor was any preferred orientation relationship evident for other silicide particles along the interface. Four experimental zone-axis diffraction patterns were obtained, presented in Figure 7(b); these zone axes are, as indicated in the figure, [001], [111], [211], and [201]. The diffraction patterns are superimposed on a quadrant of the (001) stereographic projection of a tetragonal crystal, which also illustrates the relation between the four orientations. The four respective simulated zone-axis diffraction patterns for the α -Nb₅Si₃ phase are shown in Figure 7(c), and they are consistent with the experimental diffraction data. The diffraction analysis revealed the silicide particle to be the low-temperature body-centered tetragonal α -Nb₅Si₃ phase, confirming prior EDS results [6, 7] that found a Nb:Si ratio consistent with Nb₅Si₃.

Although EDS analysis indicated differing Nb:Si ratios in the silicides at and slightly away from the ceramic-interlayer interface, no difference in their crystal structures was evident. The small size of intergranular silicides, combined with the lack of a preferred orientation relationship between the silicide and either of the adjoining, misoriented Al₂O₃ grains, introduced diffraction from the surrounding Al₂O₃ matrix that complicated diffraction analysis. Figure 8 shows bright-field and dark-field images of a small silicide particle \approx 500 nm from the Al₂O₃-interlayer interface. Diffraction patterns revealed this particle to also be the α -Nb₅Si₃ phase. The images were obtained by tilting

into a (200) systematic row condition from the [001] zone axis, as shown in the diffraction patterns inset in the figures.

In view of the presence of Nb, Si, and, to a more limited degree, Cu in the silicide particles, the Nb:Si ratios and the overall compositions were assessed in the context of the available Nb-Si and Nb-Si-Cu phase diagrams. The measured Nb:Si ratios, 1.35 and 1.21, place the composition within the two-phase field between Nb_5Si_3 and NbSi_2 on the binary equilibrium phase diagram. Two experimental studies [24, 25] of phase equilibria in the Nb-Si-Cu system are available. Experimental evidence indicates that Nb_5Si_3 can incorporate up to 12 at.% Cu at 1500°C [24]. At 1500°C, the nominal silicide compositions lie in the two-phase field between Nb_5Si_3 and NbSi_2 on the ternary phase diagram (Figure 2), close to the Nb_5Si_3 single-phase region. As the temperature is decreased, phase boundary shifts are expected. The maximum Cu solubility in the Nb_5Si_3 phase at 1100°C was estimated as 4 at.%. The 875°C and 800°C isothermal sections suggest changes in the nature of the phases that would coexist in a system having the nominal particle compositions, and a substantially lower solubility of Cu in Nb_5Si_3 than at 1500°C. At 875°C, the compositions would lie in a three-phase stability field of Nb_5Si_3 , NbSi_2 , and a ternary liquid; the phase diagram suggests a solubility limit of Cu in Nb_5Si_3 of ≈ 2 at.% [25]. At 800°C, the nominal compositions would lie in a three-phase stability field of Nb_5Si_3 , NbSi_2 , and Cu_3Si , with the Nb_5Si_3 phase incorporating up to ≈ 2 –3 at.% Cu [25].

The EDS results, when assessed in the context of available phase diagrams, predict a multiphase equilibrium microstructure. However, evidence of silicide phases other than the Nb_5Si_3 phase was not found using electron diffraction. Contrast in bright-field images also did not reveal a second silicide phase, either within the Nb_5Si_3 particles or at the interfaces between Nb_5Si_3 particles with the Al_2O_3 and Nb. Several factors are likely to contribute to this apparent disparity between the observations and expectations based on equilibrium. The phase diagram assessments (1500°C, 875°C, and 800°C

sections) did not include compositions lying in the “Nb₅Si₃-NbSi₂” two-phase region. Thus, there is uncertainty in the limits of the Nb₅Si₃ phase stability field in the ternary diagram. However, a more significant source of error will stem from difficulties in obtaining quantitative EDS data from small, dispersed silicide phases within a matrix phase (surrounding Nb and Al₂O₃), leading to large uncertainty in the measured compositions. This will cause shifts in the apparent compositions of the silicide particles. Previously [20], compositions of binary silicides were determined by assuming an exact stoichiometry to calculate *k*-factors, thus providing a range of compositions that fit this stoichiometry. Furthermore, the analysis of a multiphase specimen in which the electron beam passes through one or more phases will lead to an incorrect measurement of composition for the phases. In prior studies [65] efforts were made to examine only silicides that projected out from the edge of the TEM foil, avoiding the complications of a multiphase analysis. In this study, it was not possible to obtain spectra from isolated silicide particles unless the silicides were at the ceramic-metal interface. The quantitative correction software makes the implicit assumption that the specimen has a composition given by the combination of all the elements present in the spectrum, which will lead to erroneous application of the ZAF corrections [66].

In parallel, one can also compare the findings to those of prior studies of niobium-silicide nucleation and growth involving Nb/Si planar reaction couples [9], bulk diffusion couples of Nb/Si and Nb/NbSi₂ [22], or the deposition of thin Nb films onto single-crystal substrates [11], followed by annealing at various temperatures. As discussed by Milanese *et al.* [22], thin-film studies can provide limited amounts of one or more components, phases may form sequentially rather than simultaneously, and interfaces may affect growth and diffusion. The discussion in the literature of the considerations that enter into determining the first phase to nucleate in thin-film structures [9, 11, 17, 18] provides an example of such effects. Nucleation energetics may favor metastable phases [20] or extend the stability field. Moreover, in the present work the Si source is a silicate

phase, the Nb is alloyed with Cu and O, and growth is along either Al₂O₃-Nb or Al₂O₃-Al₂O₃. Thus, chemical differences and microstructural factors may also play a role.

As described previously, changes in the bonding temperature from 1150°C to 1400°C, changes in the atmosphere during bonding or post-bonding anneals, increases in the Cu film thickness, and changes in fracture test method all appear to influence the dominant path of crack propagation in these materials. Depending upon the bonding and test conditions, significant tearing of the Nb foil, propagation of the crack along the ceramic-interlayer interface, or significant excursions into the Al₂O₃ was observed.

Several studies have revealed that the interfacial silicides tend to form most easily in the finer-grained regions of the Al₂O₃. In view of the bimodal character of the Al₂O₃ grain size, this suggests that a substantial fraction of the total interface could potentially include silicide particles. This is consistent with the relative ease of finding the particles in TEM cross-sections. A reduced milling rate relative to Cu is also expected, which facilitates observation. The microscopy indicates that the Nb₅Si₃ grows both laterally along the ceramic-metal interface and into the Al₂O₃ along grain boundaries. As shown in this study and prior work [6, 7, 48], the silicides do not provide a continuous, low-energy fracture path. The silicides are, however, effective in altering the crack path when fracture occurs at or near the ceramic-interlayer interface.

In cases where the fracture has involved excursions of the crack front into the metal foil, one can speculate that the failure proceeded through the patches of silicide along the ceramic-metal interface that extend into the metal. Nb₅Si₃ is known to be brittle, and the fracture toughness has been reported to be between 2.3–5.5 MPa√m [42, 43]. Equilibration of the silicide with the adjoining niobium foil will increase the Si levels and locally harden the niobium. EDS results are unlikely to be sufficiently accurate to distinguish between a failure that propagates through the silicide, along the interface, or deviates to a limited extent into the Si-saturated niobium.

In assessing the fatigue behavior, Kruzic *et al.* [6] observed that cracks repeatedly extended into the Al_2O_3 but were drawn back to the interface. It was concluded that although the modulus mismatch between Al_2O_3 and Nb would draw the crack to the interface, the lower intrinsic fatigue-crack propagation resistance of some Al_2O_3 grain boundaries allowed the crack to deviate into the ceramic. Preexistent flaws were implicated as possibly expediting these excursions. It appears possible, based on observations in this study, that in addition to pores or near-interfacial pockets of glassy phase, silicide particles located along grain boundaries could also serve as “preexistent flaws.” In addition to having low fracture toughness, the coefficient of thermal expansion of Nb_5Si_3 is reported to be $6.2 \times 10^{-6} \text{ K}^{-1}$ [43], and thus lower than that of Al_2O_3 ($\approx 8.2 \times 10^{-6} \text{ K}^{-1}$). Both the portions of the Nb_5Si_3 that extend parallel to the Al_2O_3 -interlayer interface and the wedge-like particles that extend down the grain boundaries would generate tensile stresses in the Al_2O_3 . Since these particles do not extend to any significant depth below the Al_2O_3 -interlayer interface, this may be a factor in keeping the cracks in the Al_2O_3 to a substantial degree and preventing more substantial deviations away from the interlayer. The lower interfacial fracture energy of Nb_5Si_3 with Al_2O_3 ($\approx 16 \text{ J/m}^2$) relative to that of Nb_5Si_3 with Nb ($\geq 34 \text{ J/m}^2$) [45] may also help to account for crack deviations into the alumina.

A much more limited set of bend tests was conducted in which the finer-grain-size 99.9%-pure Al_2O_3 was bonded with Cu/Nb/Cu interlayers for varying times (5 min, 30 min, 6 h) at 1400 °C. For the 6-h samples [50], a limited number of room-temperature tests resulted in exclusively ceramic failure and an average fracture strength of $\approx 360 \text{ MPa}$ (versus 240 MPa for the 99.5%-pure Al_2O_3). The transition to ceramic failure suggests a substantial strengthening of the ceramic-interlayer interface. Whether this is a consequence of fewer or less severe flaws along or near the interface as a result of grain-size refinement and altered Cu-particle characteristics or whether this may in part be due to the lack of periodic arrays of silicide particles is uncertain. Further studies of this

behavior that would improve the statistics would be useful, as would more detailed fracture studies. In a system where fracture can involve a wide range of homophase and heterophase interfaces ($\text{Al}_2\text{O}_3/\text{Nb}$, $\text{Al}_2\text{O}_3/\text{Nb}_5\text{Si}_3$, $\text{Al}_2\text{O}_3/\text{Cu}$, $\text{Nb}/\text{Nb}_5\text{Si}_3$, Nb/Cu , and $\text{Nb}_5\text{Si}_3/\text{Cu}$), understanding microstructural effects and the character of phases that are present becomes a necessary precursor toward fabricating strong, reliable ceramic-metal interfaces.

4. SUMMARY

Prior work, based largely on optical and scanning electron microscopy, suggested that Al_2O_3 -Nb interfaces processed with single-crystal sapphire or high-purity, polycrystalline Al_2O_3 were free of secondary phases. In contrast, interfaces fabricated with a lower-purity, polycrystalline Al_2O_3 formed Nb silicide particles along the Al_2O_3 -Nb interface and Al_2O_3 grain boundaries. In the present work, TEM-based methods were used to examine these interfaces at higher spatial resolution, and to provide a more detailed and complete characterization of the crystallographic and chemical characteristics of secondary phases that were present.

The TEM results confirm the absence of silicides (and other secondary phases) in both the sapphire and high-purity Al_2O_3 samples, and the presence of silicides when lower-purity Al_2O_3 is used. Diffraction analysis of a silicide particle at the Al_2O_3 -Nb interface revealed that the silicide was the body-centered tetragonal α - Nb_5Si_3 phase. Energy-dispersive spectrometry of silicides both at and slightly away from the interface showed that the range of Nb:Si ratios would place the composition in the two-phase region between Nb_5Si_3 and NbSi_2 on the binary Nb-Si phase diagram at all temperatures from the 1400°C processing temperature down to room temperature. However, evidence for a two-phase structure was not found. The silicide incorporates a small amount of Cu, which modifies the phase-stability field, and may extend the stability range of the “ α - Nb_5Si_3 ” structure. Unfortunately, the only isothermal sections available are at temperatures above (1500°C) or well below (875°C, 800°C) the joining temperature. The ternaries also suggest a multiphase microstructure should form. The difficulties of quantitative EDS for small dispersed phases of the type examined and resulting shifts in the apparent composition of the silicide, as well as the role of kinetic barriers to achieving equilibrium in severely constrained systems, emerge as possible explanations for the disparity. Studies of samples subjected to longer anneals and phase equilibria studies of

relevant Nb-Si-Cu compositions at intermediate temperatures would provide useful insights on the origins of the observed microstructures.

ACKNOWLEDGMENTS

This research was supported by the U.S. Department of Energy under Contract No. DE-AC03-76SF00098. The authors acknowledge the support of the staff and facilities at the National Center for Electron Microscopy at Lawrence Berkeley National Laboratory, funded by the U.S. Department of Energy under Contract No. DE-AC02-05CH11231. AMG acknowledges generous financial support from the GRF. Work at LLNL was performed under the auspices of the U.S. Department of Energy, Office of Basic Energy Sciences, Division of Materials Sciences and Engineering, by Lawrence Livermore National Laboratory under Contract DE-AC52-07NA27344.

REFERENCES

- [1] R. M. Cannon, D. Korn, G. Elssner and M. Rühle, *Acta Mater.* 50 (2002) 3903.
- [2] G. Elssner, D. Korn and M. Rühle, *Scr. Metall. Mater.* 31 (1994) 1037.
- [3] G. Elssner, S. Reidel and R. Pabst, *Prakt. Metallogr.* 12 (1975) 234.
- [4] D. Korn, G. Elssner, R. M. Cannon and M. Rühle, *Acta Mater.* 50 (2002) 3881.
- [5] D. Korn, G. Elssner, H. F. Fischmeister and M. Rühle, *Acta Metall. Mater.* 40 (1992) S355.
- [6] J. J. Kruzic, R. A. Marks, M. Yoshiya, A. M. Glaeser, R. M. Cannon and R. O. Ritchie, *J. Am. Ceram. Soc.* 85 (2002) 2531.
- [7] J. T. McKeown, J. D. Sugar, R. Gronsky and A. M. Glaeser, *Mater. Charact.* 57 (2006) 50.
- [8] J. W. Cahn, *Acta Metall.* 4 (1956) 449.
- [9] M. Ronay, *Appl. Phys. Lett.* 42 (1983) 577.
- [10] B. Y. Tsaur, S. S. Lau, J. W. Mayer and M.-A. Nicolet, *Appl. Phys. Lett.* 38 (1981) 922.
- [11] R. M. Walser and R. W. Bené, *Appl. Phys. Lett.* 28 (1976) 624.
- [12] T. B. Massalski, H. Okamoto, P. R. Subramanian and L. Kacprzak, eds., *Binary Alloy Phase Diagrams* (ASM International, Materials Park, OH, 1990).
- [13] R. Pretorius, *Mater. Res. Soc. Symp. Proc.*, 25 (1984) 15.
- [14] R. Pretorius, *Vacuum*, 41 (1990) 1038.
- [15] R. Pretorius, R. de Reus, A. M. Vredenberg and F. W. Saris, *Mater. Lett.* 9 (1990) 494.
- [16] R. Pretorius, A. M. Vredenberg, F. W. Saris and R. de Reus, *J. Appl. Phys.* 70 (1991) 3636.
- [17] M. Zhang and W. K. Wang, *J. Mater. Res.* 13 (1998) 1373.
- [18] M. Zhang, W. Yu, W. H. Wang and W. K. Wang, *Thin Sol. Films* 289 (1996) 180.
- [19] D. Van Heerden, A. J. Gavens, T. Foecke and T. P. Weihs, *Mater. Sci. Eng. A* 261 (1999) 212.
- [20] R. J. Grylls, B. P. Bewlay, H. A. Lipsitt and H. L. Fraser, *Phil. Mag. A* 81 (2001) 1967.
- [21] G. M. Cheng, H. Y. Qian, L. L. He and H. Q. Ye, *Phil. Mag.* 90 (2010) 2557.
- [22] C. Milanese, V. Buscaglia, F. Maglia and U. Anselmi-Tamburini, *Acta Mater.* 51 (2003) 4837.
- [23] N. Mattoso Filho, C. Achete and F. L. Freire, *Thin Sol. Films* 220 (1992) 184.
- [24] V. M. Pan, V. I. Latysheva, O. G. Kulik and A. G. Popov, *Russ. Metall.* 3 (1982) 167.
- [25] R. Zankl and R. Malter, *Z. Metallk.* 72 (1981) 720.
- [26] E. Ganglberger, *Monatsh. Chem.* 99 (1968) 549.
- [27] C. Brukl, H. Nowotny and F. Benesovsky, *Monatsh. Chem.* 92 (1961) 967.
- [28] T. Murakami, S. Sasaki, K. Ichikawa and A. Kitahara, *Intermetallics* 9 (2001) 621.
- [29] T. Murakami, S. Sasaki, K. Ichikawa and A. Kitahara, *Intermetallics* 9 (2001) 629.

- [30] V. M. Pan, V. I. Latysheva, O. G. Kulik, A. G. Popov and E. N. Litvinenko, *Russ. Metall.* (1984) 233.
- [31] J. C. Zhao, L. A. Peluso, M. R. Jackson and L. Z. Tan, *J. Alloys Compd.* 360 (2003) 183.
- [32] A. Bartlett, A. G. Evans and M. Rühle, *Acta Metall. Mater.* 39 (1991) 1579.
- [33] J. R. Rice, *J. Appl. Mech.* 55 (1988) 98.
- [34] J. R. Rice and G. C. Sih, *J. Appl. Mech.* 32 (1965) 418.
- [35] G. C. Sih and J. R. Rice, *J. Appl. Mech.* 31 (1964) 477.
- [36] J. Dundurs, *J. Appl. Mech.* 36 (1969) 650.
- [37] Z. Suo and J. W. Hutchinson, *Mater. Sci. Eng. A* 107 (1989) 135.
- [38] J. W. Hutchinson, M. E. Mear and J. R. Rice, *J. Appl. Mech.* 54 (1987) 828.
- [39] T. L. Becker, J. M. McNaney, R. M. Cannon and R. O. Ritchie, *Mech. Mater.* 25 (1997) 291.
- [40] J. M. McNaney, R. M. Cannon and R. O. Ritchie, *Int. J. Fract.* 66 (1994) 227.
- [41] R. O. Ritchie, R. M. Cannon, B. J. Dalgleish, R. H. Dauskardt and J. M. McNaney, *Mater. Sci. Eng. A* A166 (1993) 221.
- [42] E. M. Carrillo-Heian, C. Unuvar, J. C. Gibeling, G. H. Paulino and Z. A. Munir, *Scr. Mater.* 45 (2001) 405.
- [43] R. K. Nekkanti and D. Dimiduk, *Mater. Res. Soc. Symp. Proc.*, 194 (1990) 175.
- [44] L. T. Zhang and J. S. Wu, *Scr. Mater.* 38 (1998) 307.
- [45] L. Shaw, D. Miracle and R. Abbaschian, *Acta Metall. Mater.* 43 (1995) 4267.
- [46] M. L. Shalz, B. J. Dalgleish, A. P. Tomsia, R. M. Cannon and A. M. Glaeser, *J. Mater. Sci.* 29 (1994) 3678.
- [47] R. A. Marks, D. R. Chapman, D. T. Danielson and A. M. Glaeser, *Acta Mater.* 48 (2000) 4425.
- [48] J. D. Sugar, J. T. McKeown, R. A. Marks and A. M. Glaeser, *J. Am. Ceram. Soc.* 85 (2002) 2523.
- [49] J. T. McKeown, J. D. Sugar, R. Gronsky and A. M. Glaeser, *Weld. J.* 84 (2005) 41S.
- [50] R. A. Marks, J. D. Sugar and A. M. Glaeser, *J. Mater. Sci.* 36 (2001) 5609.
- [51] M. L. Shalz, B. J. Dalgleish, A. P. Tomsia and A. M. Glaeser, *J. Mater. Sci.* 29 (1994) 3200.
- [52] R. Dauskardt, M. Lane, Q. Ma and N. Krishna, *Eng. Fract. Mech.* 61 (1998) 141.
- [53] J. D. Sugar, J. T. McKeown, T. Akashi, S. M. Hong, K. Nakashima and A. M. Glaeser, *J. Eur. Ceram. Soc.* 26 (2006) 363.
- [54] M. Rühle, *J. Eur. Ceram. Soc.* 16 (1996) 353.
- [55] M. Rühle and A. G. Evans, *Mater. Sci. Eng. A* 107 (1989) 187.
- [56] K. Burger, W. Mader and M. Rühle, *Ultramicroscopy* 22 (1987) 1.
- [57] M. Florjancic, W. Mader, M. Rühle and M. Turwitt, *J. Phys. (Paris)* 46 (1985) 129.
- [58] W. Mader and M. Rühle, *Acta Metall.* 37 (1989) 853.
- [59] I. Barin, *Thermochemical Data of Pure Substances* (VCH Publishers, New York, 1995).
- [60] R. A. Marks, M.S. Thesis, University of California, Berkeley, 2000.
- [61] R. A. Perkins and R. A. Padgett, *Acta Metall.* 25 (1977) 1221.

- [62] M. E. Schlesinger, H. Okamoto, A. B. Gokhale and R. Abbaschian, *J. Phase Equil.* 14 (1993) 502.
- [63] P. Villars and L. D. Calvert, *Pearson's Handbook of Crystallographic Data for Intermetallic Phases* (ASM International, Materials Park, OH, 1991).
- [64] J. Geng, P. Tsakirooulos and G. S. Shao, *Intermetallics* 15 (2007) 69.
- [65] B. Cockeram, M. Saqib, R. Omlor, R. Srinivasan, L. E. Matson and I. Weiss, *Scr. Metall. Mater.* 25 (1991) 393.
- [66] J. C. Russ, *Fundamentals of Energy Dispersive X-Ray Analysis* (Butterworths & Co, Ltd., London, 1984).
- [67] T. B. Massalski, H. Okamoto, P. R. Subramanian and L. Kacprzak, eds., *Binary Alloy Phase Diagrams* (ASM International, Metal Parks, OH, 1990).
- [68] V. M. Pan, V. I. Latysheva, O. G. Kulik and A. G. Popov, *Russ. Metall.* 3 (1982) 167.
- [69] P. Villars, A. Prince and H. Okamoto, eds., *Handbook of Ternary Alloy Phase Diagrams* (ASM International, Materials Park, OH, 1995).
- [70] P. Villars, A. Prince and H. Okamoto, eds., *Handbook of Ternary Alloy Phase Diagrams* (ASM International, Materials Park, OH, 1995).

FIGURE CAPTIONS

- Figure 1:** Niobium-silicon equilibrium binary phase diagram. Reproduced after reference [67].
- Figure 2:** Ternary niobium-silicon-copper equilibrium phase diagram at 1500°C. Single-phase regions are shaded dark gray and labeled, two-phase regions are white, and three-phase regions are shaded light gray. Reproduced after reference [68, 69].
- Figure 3:** (a) Bright-field TEM images of (a) a (0001) sapphire–niobium interface, (b) a high-purity alumina–niobium interface (note the preferential thinning at the interface), and (c) a lower-purity alumina–niobium interface revealing the presence of niobium silicides. In both polycrystalline alumina samples, the niobium has conformed to the alumina grain boundaries and penetrated into the grain-boundary grooves.
- Figure 4:** (a) EDS line scan across a silicide particle at the alumina–niobium interface, and (b) spectra from different regions of the particle. When normalized by the niobium counts to minimize thickness effects, (a) the copper and silicon concentrations are constant across the scanned region of the particle and (b) the four spectra overlap. The dashed line in (b) indicates the interface between the niobium and the silicide particle.
- Figure 5:** EDS line scan across a small silicide particle on an alumina grain boundary, showing the presence of niobium, silicon, and copper.
- Figure 6:** EDS spectrum obtained from a silicide particle along an alumina grain boundary away from the alumina–niobium interface.
- Figure 7:** (a) Bright-field TEM image of the silicide particle from which the diffraction patterns in (b) were obtained. The image was recorded in the [001] zone axis. (b) Experimental and (c) simulated [001], [111], [211], and [201] zone-axis diffraction patterns for the particle shown in (a), superimposed on a quadrant of the (001) stereographic projection for a tetragonal crystal, revealing that the particle is the body-centered tetragonal Nb₅Si₃ phase.
- Figure 8:** (a) Bright-field and (b) dark-field TEM images of a silicide particle at an alumina grain boundary.

FIGURES

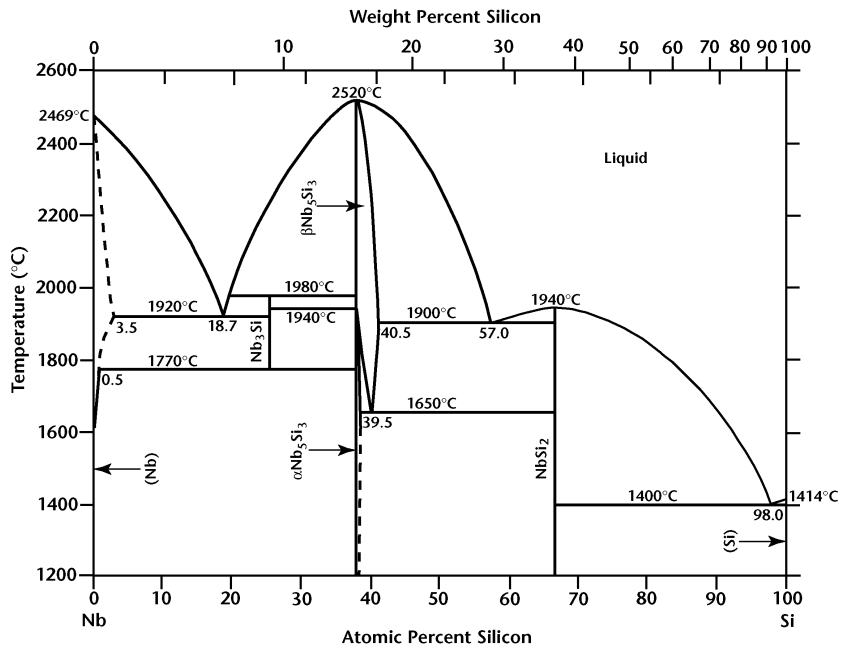


Figure 1: Niobium-silicon equilibrium binary phase diagram. Reproduced after reference [67].

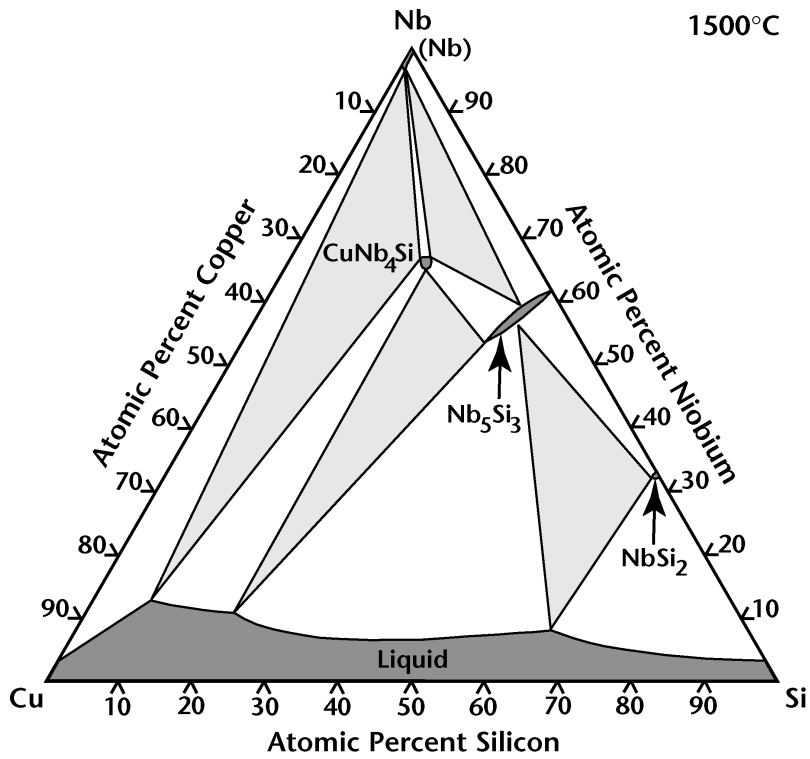


Figure 2: Ternary niobium-silicon-copper equilibrium phase diagram at 1500°C. Single-phase regions are shaded dark gray and labeled, two-phase regions are white, and three-phase regions are shaded light gray. Reproduced after reference [24, 70].

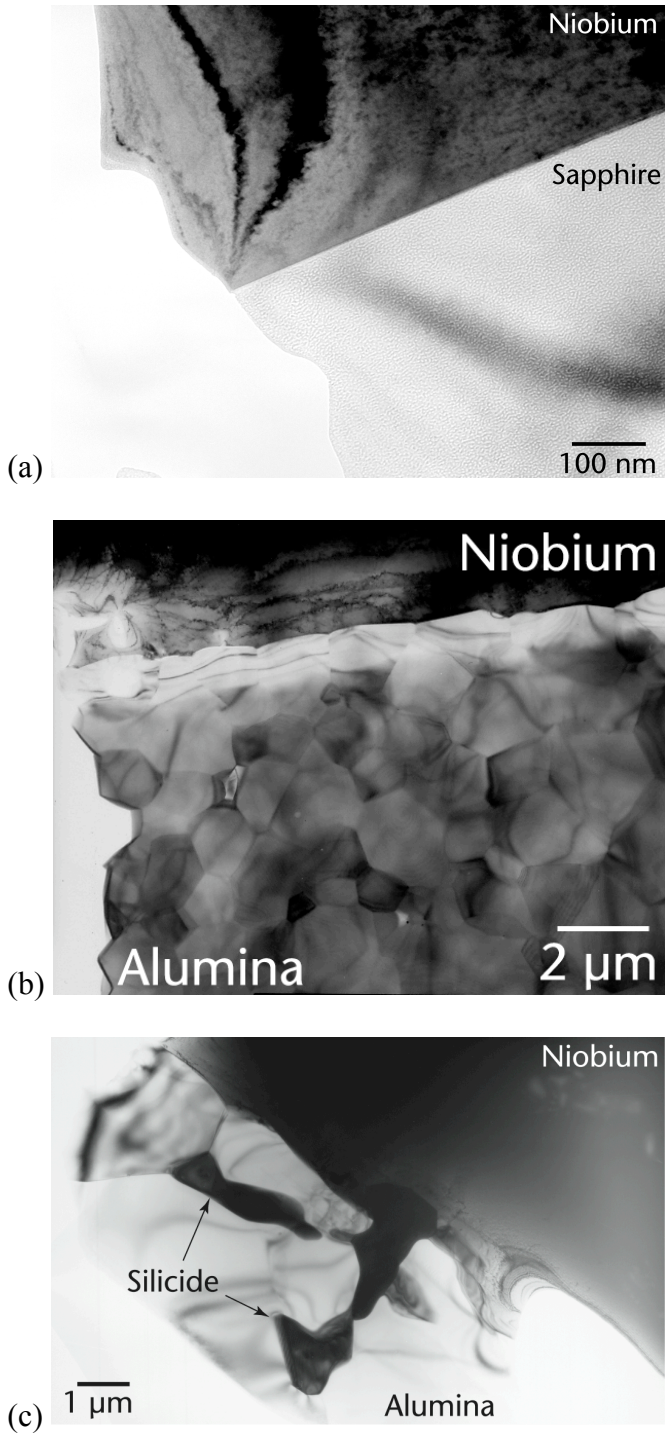


Figure 3: (a) Bright-field TEM images of (a) a (0001) sapphire–niobium interface, (b) a high-purity alumina–niobium interface (note the preferential thinning at the interface), and (c) a lower-purity alumina–niobium interface revealing the presence of niobium silicides. In both polycrystalline alumina samples, the niobium has conformed to the alumina grain boundaries and penetrated into the grain-boundary grooves.

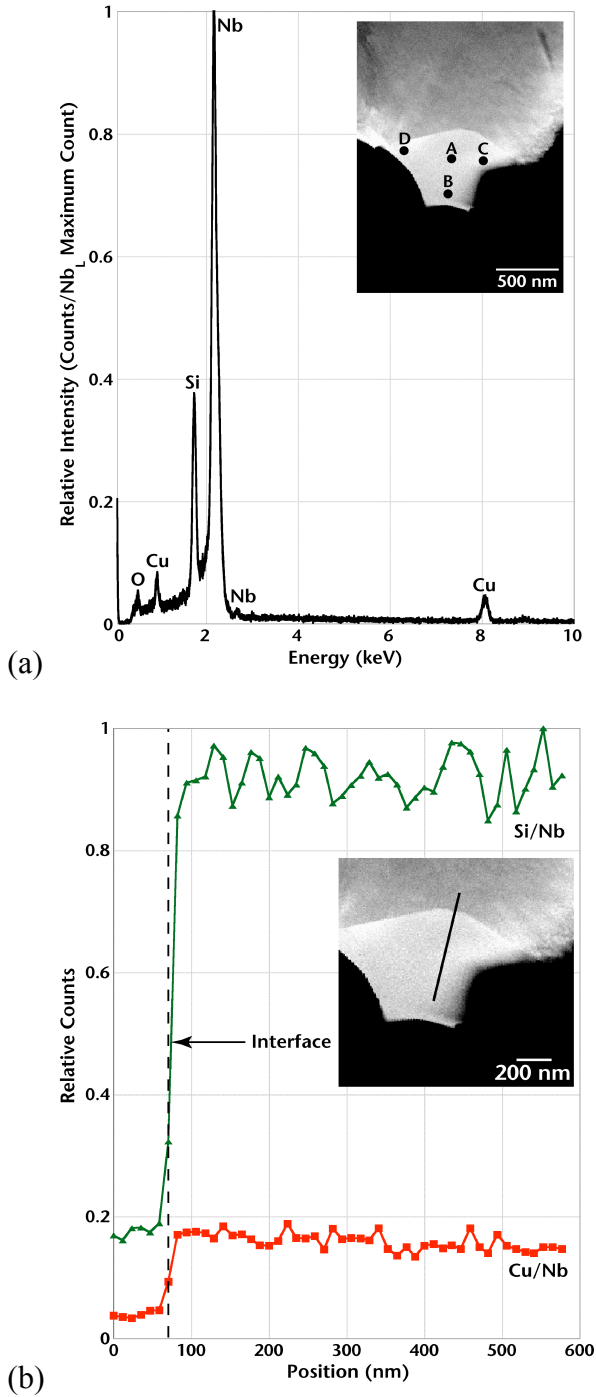


Figure 4: (a) EDS line scan across a silicide particle at the alumina-niobium interface, and (b) spectra from different regions of the particle. When normalized by the niobium counts to minimize thickness effects, (a) the copper and silicon concentrations are constant across the scanned region of the particle and (b) the four spectra overlap. The dashed line in (b) indicates the interface between the niobium and the silicide particle.

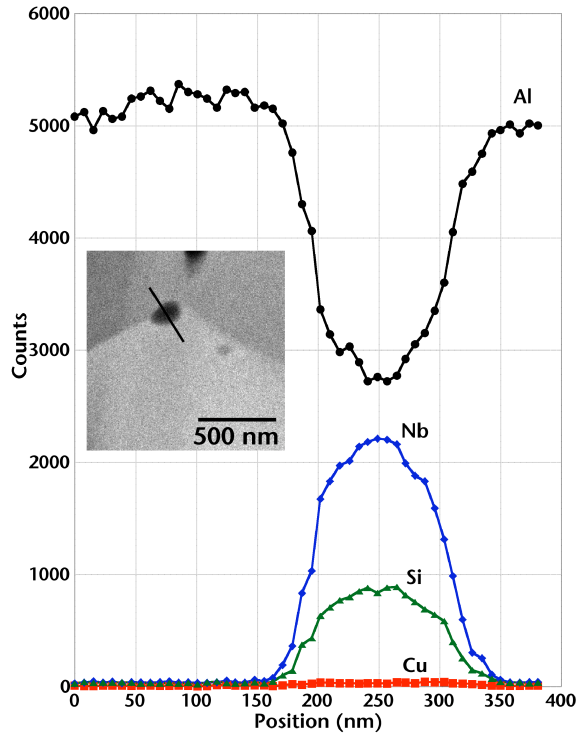


Figure 5: EDS line scan across a small silicide particle on an alumina grain boundary, showing the presence of niobium, silicon, and copper.

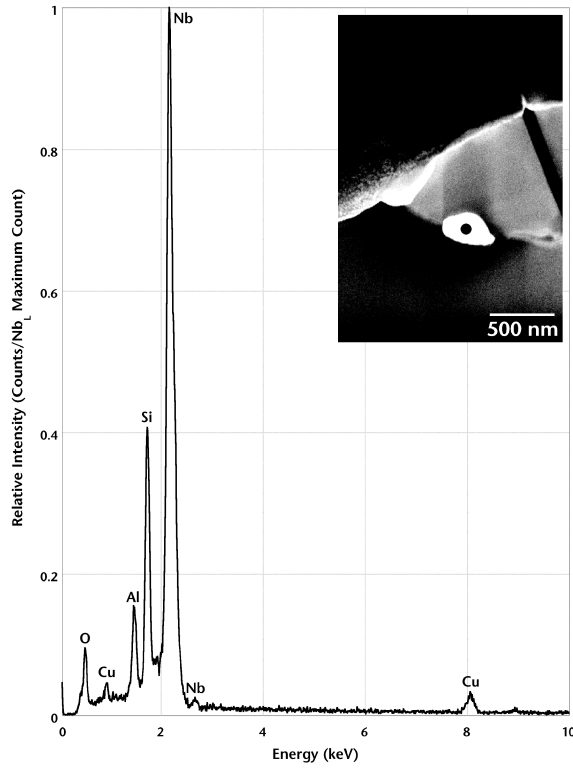
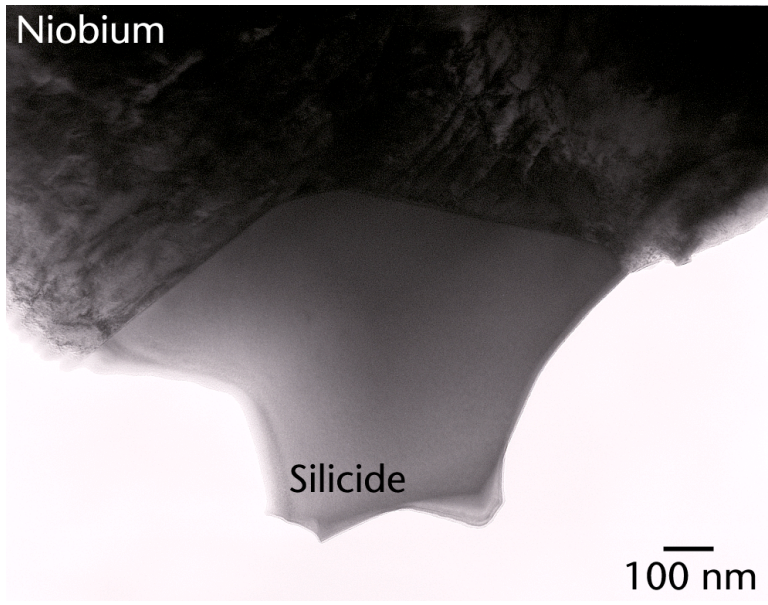
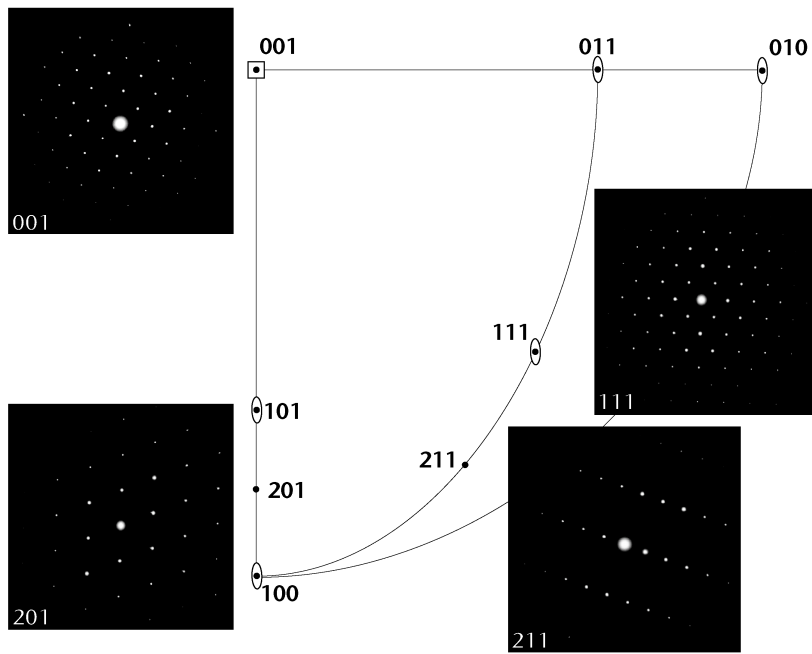


Figure 6: EDS spectrum obtained from a silicide particle along an alumina grain boundary away from the alumina-niobium interface.



(a)



(b)

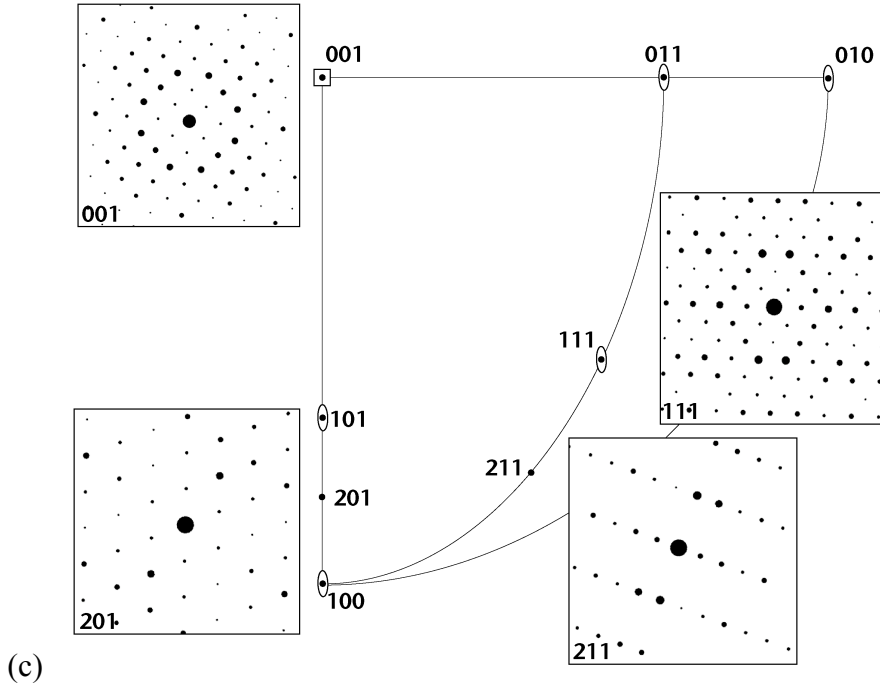


Figure 7: (a) Bright-field TEM image of the silicide particle from which the diffraction patterns in (b) were obtained. The image was recorded in the [001] zone axis. (b) Experimental and (c) simulated [001], [111], [211], and [201] zone-axis diffraction patterns for the particle shown in (a), superimposed on a quadrant of the (001) stereographic projection for a tetragonal crystal, revealing that the particle is the body-centered tetragonal Nb_5Si_3 phase.

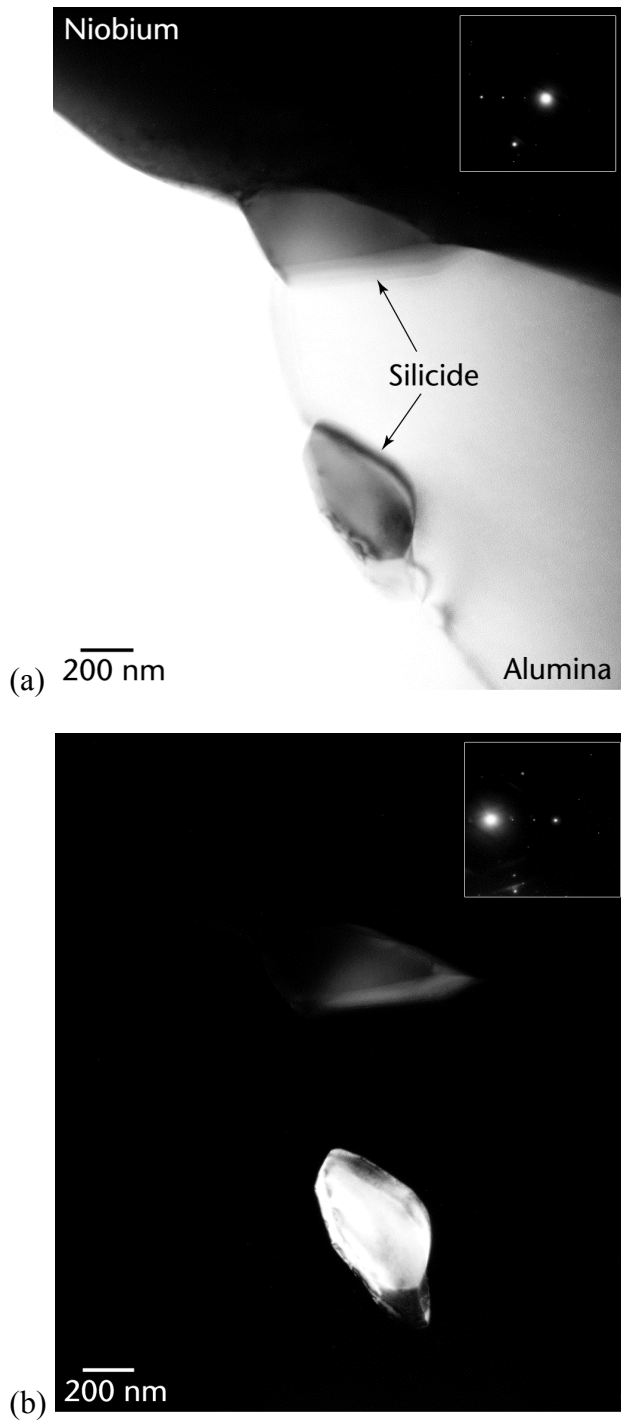


Figure 8: (a) Bright-field and (b) dark-field TEM images of a silicide particle at an alumina grain boundary.